

# Inherent Structures for Soft Long-Range Interactions in Two-Dimensional Many-Particle Systems

Robert D. Batten,<sup>1</sup> Frank H. Stillinger,<sup>2</sup> and Salvatore Torquato<sup>2,3,4,5</sup>

*<sup>1</sup>Department of Chemical Engineering,  
Princeton University, Princeton, NJ 08544, USA*

*<sup>2</sup>Department of Chemistry, Princeton University, Princeton, NJ, 08544 USA*

*<sup>3</sup>Princeton Center for Theoretical Science,  
Princeton University, Princeton, NJ 08544, USA*

*<sup>4</sup>Program in Applied and Computational Mathematics,  
Princeton University, Princeton, NJ 08544, USA*

*<sup>5</sup>Princeton Institute for the Science and Technology of Materials,  
Princeton University, Princeton, NJ 08544, USA\**

(Dated: November 27, 2018)

## Abstract

We generate inherent structures, local potential-energy minima, of the “ $k$ -space overlap potential” in two-dimensional many-particle systems using a cooling and quenching simulation technique. The ground states associated with the  $k$ -space overlap potential are stealthy (*i.e.*, completely suppress single scattering of radiation for a range of wavelengths) and hyperuniform (*i.e.*, infinite wavelength density fluctuations vanish). However, we show via quantitative metrics that the inherent structures exhibit a range of stealthiness and hyperuniformity depending on the fraction of degrees of freedom that are constrained. Inherent structures in two dimensions typically contain five-particle rings, wavy grain boundaries, and vacancy-interstitial defects. The structural and thermodynamic properties of inherent structures are relatively insensitive to the temperature from which they are sampled, signifying that the energy landscape is relatively flat and devoid of deep wells. Using the nudged-elastic-band algorithm, we construct paths from ground-state configurations to inherent structures and identify the transition points between them. In addition, we use point patterns generated from a random sequential addition (RSA) of hard disks, which are nearly stealthy, and examine the particle rearrangements necessary to make the configurations absolutely stealthy. We introduce a configurational proximity metric to show that only small local, but collective, particle rearrangements are needed to drive initial RSA configurations to stealthy disordered ground states. These results lead to a more complete understanding of the unusual behaviors exhibited by the family of “collective-coordinate” potentials to which the  $k$ -space overlap potential belongs.

## I. INTRODUCTION

Recently, we have been interested in a family of soft, long-range pair interactions that give rise to novel physical behaviors of many-particle systems including classical disordered ground states for a range of densities, negative thermal expansion, and vanishing normal-mode frequencies.<sup>1-4,4-6</sup> This family of soft pair interactions includes those pair potentials  $v(r)$  with Fourier transforms  $V(k)$  that are positive, bounded, and vanish to zero at some finite wavenumber  $K$  and beyond. The potential energy  $\Phi$  of a system of  $N$  particles in a fundamental cell with volume  $\Omega$  under periodic boundary conditions can be written as

$$\phi = \Phi/N = \frac{1}{N} \sum_{j>i}^N v(\mathbf{r}_{ij}), \quad (1)$$

$$= \frac{1}{2\Omega} \sum_{\mathbf{k}} V(\mathbf{k}) [\rho(\mathbf{k})\rho(-\mathbf{k})/N - 1], \quad (2)$$

where  $r_{ij} \equiv |\mathbf{r}_i - \mathbf{r}_j|$  is the distance between particles  $i$  and  $j$ ,  $\rho(\mathbf{k})$  are the Fourier coefficients of the density field, and  $\mathbf{k}$  are the wave vectors appropriate for the system size and shape. These soft pair interactions, called “collective-coordinate” potentials, are bounded and possess long-range oscillations in real space.<sup>5</sup>

Because of the finite cutoff in  $k$ -space, an analytic lower bound for the potential energy per particle  $\phi$  is easily obtainable, and numerical methods allow for the construction and investigation of ground states with extremely high precision. A series of studies has examined the structural characteristics of ground states in one,<sup>7</sup> two,<sup>8</sup> and three dimensions.<sup>4</sup> Three structural ground-state regimes were found to characterize these two-dimensional systems. Increasing the fraction of degrees of freedom that are constrained  $\chi$ , equivalently decreasing density, spans regimes that are disordered, wavy-crystalline, and crystalline. Recently, an analytical connection between the fraction of constrained degrees of freedom within the system and the disorder-order phase transition for a class of target structure factors has been provided<sup>9</sup> by examining the realizability of the constrained contribution to the pair correlation function.

More recently, these potentials were used to construct “stealthy” and “hyperuniform” materials in two dimensions.<sup>3</sup> “Stealthy” materials refer to point patterns that completely suppress single scattering of radiation for certain wavelength ranges. While nonstealthy materials may allow for some small amount of scattering, stealthy materials are absolutely

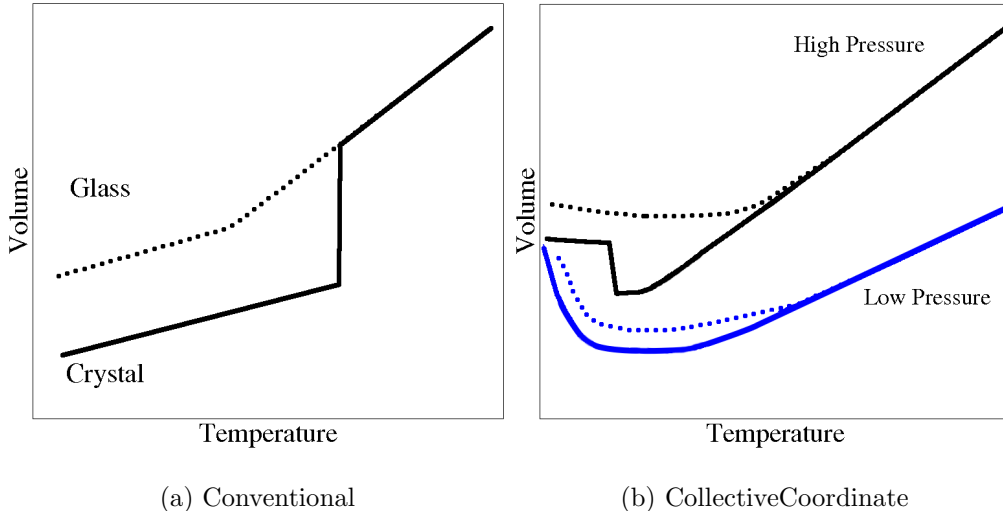


FIG. 1: (Color online) Schematics of the equilibrium equation of state (solid lines) and the nonequilibrium path that results in glassy behavior (dotted lines) along an isobar. With familiar potentials (*e.g.* Lennard-Jones) (left), the equilibrium curve shows a first-order phase transition while the glassy curve undergoes supercooling and a glass transition. With the soft, long range  $k$ -space overlap potential (right), high-pressure systems result in a first-order transition that is not present for low-pressure systems. Both collective-coordinate systems undergo negative thermal expansion.

transparent at those wavelengths. “Hyperuniform” refers to point patterns in which infinite wavelength density fluctuations vanish.<sup>10</sup> (These terms are defined more precisely in Sec. II.) The hyperuniformity notion enables the rank ordering of crystals, quasicrystals and special disordered many-particle systems.<sup>10–12</sup> Interestingly, disordered hyperuniform many-particle ground states, and therefore also point distributions, with substantial clustering can be constructed.<sup>9</sup>

Constructed ground states are now the basis for novel disordered materials with tunable, photonic band gaps.<sup>13,14</sup> Using a model potential from the family of collective-coordinate potentials in two dimensions, the “ $k$ -space overlap potential,” described in Sec. II, we observed negative thermal expansion and vanishing normal-mode frequencies for ground-state configurations. We attributed these phenomena to the nature of the underlying energy landscape, which we described as having ground-state “valleys” that weave between the higher-energy portions of the landscape.<sup>1,2</sup>

Despite the discovery of the existence of such unique properties, the fundamental mechanisms allowing for disordered ground states and stealthy point patterns still need to be fully

elucidated. Here, we analyze the energy landscape further by examining the associated inherent structures, or local potential-energy minima, for the aforementioned  $k$ -space overlap potential in two dimensions to better understand these properties.

We have two primary motivations for this work. First, through the course of our previous research, we have observed several paradoxical phenomena related to local potential-energy minima and glassy behavior. While an “inherent structure” is in general any local potential-energy minimum, the term “glass” refers to an amorphous solid that is kinetically trapped in a potential-energy well. In Ref. [2], we observed an unusual equation of state when cooling a system compared to a more familiar (*e.g.*, Lennard-Jones) glass-forming system as Fig. 1 demonstrates this schematically. In Fig. 1(a), the dark and dotted lines represent the equilibrium equation of state and nonequilibrium isobaric cooling path for a Lennard-Jones system. Figure 1(b) shows the corresponding cooling paths for a system interacting with the  $k$ -space overlap potential. In the more familiar glass-forming system, there is a well-defined glass transition below the freezing point that is dependent on the rate at which the system is cooled.<sup>15</sup> It is well known that the glass-forming behavior of a system is a function of the underlying energy landscape.<sup>16</sup> The depths of the potential-energy wells in the energy landscape dictate the dynamics of structural rearrangements of the system.<sup>17,18</sup> For the  $k$ -space overlap potential, we observed that at high pressure the nonequilibrium curve deviated from the equilibrium curve at a temperature above the melting temperature, as demonstrated in Fig. 1(b). At lower pressures where there is no well-defined melting temperature, as in the wavy-crystalline regime, the nonequilibrium curve deviates similarly from the equilibrium curve. In addition, the  $k$ -space overlap potential gives rise to negative thermal expansion, generally for nondimensional  $T^* < 0.0007$ .<sup>1,2</sup>

Other paradoxical behaviors have led us toward a broad analysis of the energy landscape. We have observed that some ground-state configurations, particularly crystalline structures, had many zero-energy normal modes. These ground states are therefore not mechanically rigid. However, while using numerical minimization algorithms to construct ground-state configurations, we encountered many mechanically stable local potential-energy minima. Lastly, there exists a large density range in which the energy landscape was evidently devoid of all local minima. An increment in  $\chi$  just outside this range introduced local potential-energy minima to the landscape.

While we have previously observed these phenomena,<sup>1-3</sup> the fundamental mechanisms

that underlie them are not fully understood. The inherent-structure analysis has proven to be a fruitful method for relating the energy landscape to low-temperature phenomena. Many studies have examined inherent-structure characteristics in glass-forming liquids with strong repulsive cores such as the Stillinger-Weber potential,<sup>19–21</sup> water-like pair potentials,<sup>22</sup> binary Lennard-Jones-like systems,<sup>23–26</sup> and general repulsive potentials.<sup>27,28</sup> The inherent structures for Lennard-Jones and steeply repulsive potentials are in general not hyperuniform or stealthy due to the dominance of grain boundaries and vacancy defects.

In contrast to the above list of strongly repelling potentials, the  $k$ -space overlap potential is a soft interaction. Soft interactions are often useful models for soft-matter systems such as colloids, polymers, and microemulsions.<sup>29</sup> In addition, these  $k$ -space overlap interactions are also qualitatively similar to Friedel oscillations in molten metals.<sup>30</sup> The  $k$ -space overlap potential is localized in  $k$ -space and delocalized in real space as a result of the Fourier transform. Certain duality relations link the ground-state energies of the  $k$ -space overlap potential to the ground-state energies of real space analog.<sup>5,31</sup> There have been several investigations of the inherent structures of various soft interactions. The Gaussian-core model in two dimensions has polycrystalline inherent structure with a large correlation length even when sampled from the liquid state.<sup>32</sup> Energy landscape analyses revealed that the range of the Morse potential affects the relation between temperature and the potential-energy distribution of sampled inherent structures.<sup>33</sup> While for the Yukawa potential, inherent structures varied depending on whether they were obtained from the liquid, crystal or hexatic phase.<sup>34</sup>

Novel, stealthy dielectric materials are currently being fabricated,<sup>14</sup> and nearly stealthy ceramic materials are of interest for optical applications.<sup>35,36</sup> Because of these recent experimental applications and the unusual physical behaviors discovered,<sup>1–3</sup> we are also motivated to understand the fundamental differences between point patterns that absolutely suppress scattering for certain wavelengths and those that nearly suppress scattering. Our ground-state construction procedure<sup>3</sup> automatically distinguishes stealthy and hyperuniform configurations from those that do not possess such properties. In particular, we want to understand whether the particle rearrangements required to transform nearly hyperuniform and stealthy materials to configurations that are perfectly hyperuniform and stealthy are global or local in nature.

While a general method for understanding these particle rearrangements would require a new algorithm to search for collective motions that increase stealthiness, the collective-

coordinate approach provides an excellent framework from which to address this question. Here, we provide two methods for identifying rearrangements in particle systems to achieve stealthy and hyperuniform materials. For large  $\chi$ , we use the nudged-elastic-band algorithm to connect inherent structures, which are nearly hyperuniform and nearly stealthy, to ground states along a minimum-energy path. For small  $\chi$  values, we have identified that there are no inherent structures higher up in the energy landscape. Therefore, we study the rearrangements from a saturated random sequential addition (RSA) of hard disks<sup>37</sup> to ground states of the  $k$ -space overlap potential. We use saturated RSA systems as initial conditions because upon saturation they suppress scattering for small wavenumbers and are nearly hyperuniform.<sup>35–37</sup> We also introduce a stealthiness metric and a configurational proximity metric to quantify characteristics of these transitions.

In this paper, we use a collective-coordinate potential and a simulation methodology to find stealthy point patterns and local potential-energy minima above the ground state. We probe the following fundamental questions:

- How are inherent structures and their thermodynamic properties in collective coordinate systems different from those found in other soft-potential systems?
- To what extent are inherent structures stealthy and/or hyperuniform?
- How are the features of inherent structures related to the pair potential function?
- What collective particle rearrangements are necessary to construct a path from an inherent structure to a ground state?
- What global and/or local particle rearrangements are necessary to convert a nearly stealthy and nearly hyperuniform system in to one that is absolutely stealthy and hyperuniform?

The remainder of this paper is organized as follows. In Sec. II, we define the  $k$ -space overlap potential, introduce several definitions, and briefly review the ground-state structural regimes. In Sec. III, we detail the methods we use to obtain and characterize inherent structures. In addition, we discuss the methods we use to find transition states between inherent structures and ground states. In Sec. IV, we examine the thermodynamic properties of inherent structures as a function of system size and cooling rate. The inherent structures are

characterized in Sec. V. Paths connecting inherent structures to ground states are provided in Sec. VI while the rearrangements from RSA systems to ground states are explored in Sec. VII. Concluding remarks are provided in Sec. VIII.

## II. COLLECTIVE COORDINATES AND THE OVERLAP POTENTIAL

While a fully detailed summary of collective coordinates is provided in Ref. [2], we provide a brief summary of the relevant mathematical relations and definitions here. Recall that the potential energy of the system of interacting particles in a periodic simulation box is defined in Eq. (1). The collective density variables  $\rho(\mathbf{k})$  are given by

$$\rho(\mathbf{k}) = \sum_{j=1}^N \exp(i\mathbf{k} \cdot \mathbf{r}_j), \quad (3)$$

where  $\mathbf{r}_j$  is the position of the  $j^{\text{th}}$  particle. The wave vectors for a periodic box correspond to linear combinations of the reciprocal lattice vectors associated with the periodic box. For a rectangular box of dimensions  $L_x$  and  $L_y$ , those wave vectors are  $\mathbf{k} = [2\pi n_x/L_x, 2\pi n_y/L_y]$ , where  $n_x$  and  $n_y$  are integers. The structure factor  $S(\mathbf{k})$ , proportional to the intensity of scattering of radiation, is related to the collective density variables via

$$S(\mathbf{k}) = \frac{\langle |\rho(\mathbf{k})|^2 \rangle}{N}, \quad (4)$$

where  $\langle \dots \rangle$  is the appropriate ensemble average. When angularly averaged, the structure factor  $S(k)$  is only dependent on the wavenumber  $k \equiv |\mathbf{k}|$ . Since the collective-coordinate class of potentials are bounded positive for  $k \leq K$  and zero for  $k > K$ , any configuration for which  $S(k)$  is constrained to be zero for all  $0 < |\mathbf{k}| < K$  is a ground state.

For such potentials, it is useful to refer to the dimensionless parameter

$$\chi = \frac{M(K)}{dN} \leq 1 \quad (5)$$

as the fraction of degrees of freedom that are constrained, where  $M(K)$  is the number of independent wave vectors  $0 < |\mathbf{k}| < K$  and  $dN$  is the total degrees of freedom.<sup>8</sup> In two dimensions  $\chi$  is limited to the range  $\chi < 0.91$ . This limit was discussed in Ref. [2] and arises from the inability to suppress Bragg scattering of the triangular lattice.<sup>38</sup> Here, we fix  $K = 1$ , and therefore  $\chi$  is inversely related to the number density  $\rho = N/\Omega$ . Some



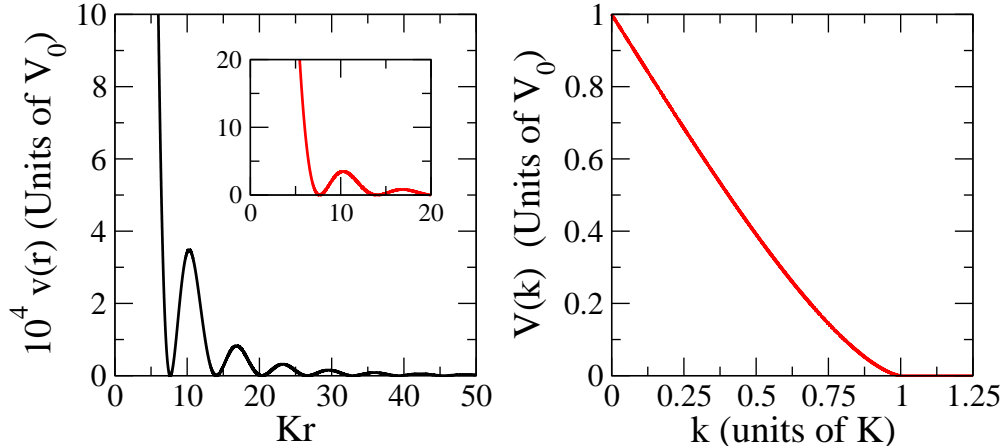


FIG. 2: The overlap pair potential function  $v(r)$  in the infinite-volume limit and its corresponding Fourier transform  $V(k)$ , the  $k$ -space overlap potential, as adapted from Ref. [2].

relations between  $\chi$  and  $\rho$  are given in Ref. [2]. Three structural regimes exist for ground-state configurations in two dimensions. For  $\chi < 0.577$ , ground states are disordered. For  $0.577 \leq \chi < 0.780$ , they are wavy crystalline, while for  $0.780 \leq \chi \leq 0.91$ , crystalline structures are the most viable ground-states configurations identified via numerical search techniques.<sup>2,8</sup> We have observed that quenching systems with  $\chi < 0.5$  always resulted in a ground state. The energy landscape is evidently devoid of local potential-energy minima above the ground state when  $\chi < 0.5$  and thus inherent-structure analysis is limited to those systems with  $\chi \geq 0.5$ .

We continue to use the  $k$ -space overlap potential, introduced by Torquato and Stillinger,<sup>5</sup> since it is exactly representable in real and reciprocal space, and is sufficiently short-ranged in real space for computational purposes; see Fig. 2. The  $k$ -space overlap potential is proportional to the intersection area between two disks of diameter  $K$  with centers separated by  $k$ , and hence for  $k \leq K$  is

$$V(k) = \frac{2V_0}{\pi} \left[ \cos^{-1} \left( \frac{k}{K} \right) - \frac{k}{K} \left( 1 - \frac{k^2}{K^2} \right)^{1/2} \right], \quad (6)$$

and zero for all  $k > K$ . In the infinite-volume limit, the associated real space pair potential is

$$v(r) = \frac{V_0}{\pi r^2} \left[ J_1 \left( \frac{Kr}{2} \right) \right]^2, \quad (7)$$

where  $J_1$  is the Bessel function. Henceforth, we refer to this  $v(r)$  as the ‘‘overlap potential.’’ The potential  $v(r)$  is bounded at  $r = 0$  and behaves as  $\cos^2(Kr/2 - 3\pi/4)/r^3$  for large  $r$ .

In this paper, we choose to report a scaled potential energy  $\varepsilon$ , omitting the structure-independent contribution at  $\mathbf{k} = 0$  and removing the additive constants, i.e.,

$$\varepsilon = \frac{1}{2\Omega} \sum_{\mathbf{k} \neq 0} V(\mathbf{k})S(\mathbf{k}), \quad (8)$$

so that ground state energies are equal to zero regardless of  $\chi$  for  $\chi < 0.91$ . This new scaled energy provides a sense as to how much a configuration differs energetically from a ground state, and is related to the actual potential energy, choosing  $V_0 = 1$ , via

$$\phi = \Phi/N = \frac{1}{\Omega N} \sum_{\mathbf{k}} [V(\mathbf{k})C(\mathbf{k})] \quad (9)$$

$$= \frac{\rho}{2} - \frac{1}{2\Omega} \sum_{\mathbf{k}} V(\mathbf{k}) + \varepsilon \quad (10)$$

Note that the structure-independent terms sum to be nonnegative because  $v(r)$  is a nonnegative function. We choose the cutoff for ground states to be those configurations in which  $\varepsilon < 10^{-10}$ .

We also compute a stealthiness metric  $\eta$  as the average of the values of the structure factor for all  $|\mathbf{k}| < K$ , defined to be

$$\eta = \sum_{0 < |\mathbf{k}| < K} S(\mathbf{k})/M(K) \quad (11)$$

This metric is a measure of the stealthiness because it vanishes to zero for completely transparent systems but will remain nonzero for nonstealthy systems. While there is a numerical limitation of  $10^{-16}$  for double precision computing, there are certain practical limits on stealthiness. Because of the weights assigned by  $V(k)$  for  $k$  near  $K$ , the metric  $\eta$  may not necessarily be suppressed to zero for ground states due to numerical precision of the quantity  $V(k)S(k)$ . Therefore, the stealthiness metric is best used as a relative comparison of stealthiness between configurations and not as a determination of a configuration as a ground state.

### III. METHODS

Our method to generate inherent structures follows that of Sastry and coworkers,<sup>18</sup> which is based on the initial algorithms of Stillinger and Weber.<sup>19,20,24</sup> Initially, we simulate the

atomic motions of the system interacting via the  $k$ -space overlap potential in Eq. (1) by integrating the Newtonian equations of motions, assuming unit mass,

$$\frac{d^2 \mathbf{r}_i}{dt^2} = -\nabla \phi. \quad (12)$$

We use the velocity Verlet algorithm<sup>39</sup> with a time step  $\delta t$  of 0.4, which is chosen so as to accurately conserve total energy in the constant  $NVE$  ensemble. Throughout the dynamical simulation, configurations were sampled and subjected to a quenching of the potential energy. Here, the sampled configuration is used as the initial condition for a conjugate gradient minimization.

Upon termination of the conjugate gradient quenching, we subject the system to an additional quenching via the MINOP algorithm.<sup>40,41</sup> We previously reported the efficiency of the MINOP algorithm compared to the conjugate gradient method.<sup>3,4</sup> We add this final quench for reasons of increased efficiency and precision compared to simply using the conjugate gradient method to high precision. Many of the inherent structures that we have found have very slight differences in the scaled potential energy  $\varepsilon$  that can be on the order of magnitude  $10^{-8}$ . Our implementation of the conjugate gradient method becomes inefficient at these tolerances. While there is a possibility that the MINOP algorithm can traverse to other capture basins, we suspect that the system is quenched sufficiently deep into a potential-energy well after the conjugate gradient step that the MINOP algorithm will not push the system into another capture basin.

We initialize the dynamical trajectories at a temperature associated with the liquid state. Here, we report the dimensionless temperature  $T^* = k_B T / V_0$ , where  $k_B$  is the Boltzmann constant and  $T$  is the simulation temperature. We previously reported that the transitions from ground states to highly disordered liquids occur in the range of  $T^* = 0.0003$ - $0.001$ , depending on  $\chi$ .<sup>2</sup> We initialize our simulations at  $T^* \geq 0.0018$ . Configurations are sampled every  $n_s$  time steps until at least fifty are obtained. Then the velocities of the system are rescaled to a lower temperature by  $dT^*$ , typically a value of 0.00015, and the configurations are sampled again at the reduced temperature. The rate at which the system is effectively cooled becomes  $\gamma = dT^* / (50n_s \delta t)$ . We have explored a range of coolings rates from  $10^{-6} \leq \gamma \leq 10^{-9}$  with  $n_s$  varying from 3 to 750. Surprisingly, as discussed in Sec. IV, while the properties of the thermal structures are sensitive to the cooling rate, the properties of the inherent structures are not.

To construct pathways between ground-state configurations and inherent structures for  $\chi > 0.5$ , we use the “nudged-elastic-band algorithm” used for finding minimum-energy transition paths.<sup>42,43</sup> This method requires as an input two local minima that are nearby in the energy landscape. We generate this pair of structures by initializing a known ground-state configuration (obtained by the search methods in Ref. [3]), assigning a small temperature to the system, and integrating the equations of motion. The configurations are quenched by the conjugate gradient/MINOP minimization every five time steps. A simulation run is terminated when the quenching of a configuration produces a local minimum in a new capture basin. This new inherent structure is presumed to be near the original ground state in configuration space.

We then apply the nudged-elastic-band (NEB) algorithm<sup>42,43</sup> to the ground state/inherent structure pair. The algorithm discretizes the path between two local minima in a potential-energy landscape into “beads,” or image configurations. These beads, representing configurations, are connected via harmonic springs of zero natural length. Then a minimization algorithm is applied to minimize simultaneously the force parallel to the string of beads and the force perpendicular to the true force. The algorithm bends the string of beads around the “hills” in the energy landscape. The end result is a discrete path that provides the minimum-energy path from one potential-energy minimum, through a low-order saddle point, and to the other potential-energy minimum. While a large number of “beads” allows for a more refined minimum-energy pathway, we find that using fifty beads serves our purposes well by yielding a smooth transition pathway and a reasonable approximation to the saddle point.

Occasionally, there are other inherent structures in the vicinity of the straight-line interpolation between the inherent structure and ground state used as an initial condition. In these cases, the NEB algorithm will not produce a smooth transition from the ground state to the original inherent structure, and therefore we refine our initial ground state/inherent structure pair. For example, when using the triangular lattice as an initial condition for say  $\chi = 0.6004$ , there are number of zero-energy modes that the system can traverse during the molecular dynamics trajectories. When applying the NEB algorithm to a triangular lattice/inherent structure pair, the pathway has a preference to bend toward the zero-energy path before moving uphill toward the saddle point. This caused the energy of the transition-state pathway to appear rugged since the string of beads was pushed near a different inherent

structure. In these cases, we searched the string of beads for a new ground-state/inherent structure pair. We minimized the potential energy of each bead until we found a new ground state/inherent structure pair closer together than the original pair and applied the NEB algorithm again. This method does not guarantee that we find the closest inherent structure to a ground state nor does it guarantee that the saddle point is a first-order (single negative eigenvalue) saddle.

For  $\chi < 0.5$ , we examine particle rearrangements from RSA configurations to ground states. To generate RSA packings, disks of diameter  $D$  are randomly, sequentially, and irreversibly placed inside a simulation cell so that they do not overlap with any other particles. The process is saturated when additional particles cannot be placed without overlapping other particles. In practice, this occurs after a very large number of attempted particle insertions are rejected. Here, we terminate the process after 1.5 million attempted particle placements. Since  $K$  is fixed to be unity, we must select a target number density  $\rho_t$  that corresponds to our target  $\chi$ . Using a desired number of particles in a saturated system of 750 particles, we then identify the appropriate system area. The simulation cell is chosen to be a square box. We can then assign the particles a diameter  $D$  so that upon saturation of the RSA process, we achieve close to the desired number density. For RSA processes in two dimensions, the saturation packing fraction  $f_s$  is 0.547.<sup>37</sup> The assigned diameter becomes  $D = 2(f_s/\pi\rho_t)^{1/2}$ . In our RSA patterns, the number of particles did not match the target number of particles due to finite system effects. Given the dimensions of the box and the number of particles, we can then assign the appropriate wave vectors and  $\chi$  value to the system. The potential energy of the system is then quenched using the conjugate gradient method followed by a quenching using the MINOP algorithm as was detailed above.

To characterize inherent structures, we use several quantitative metrics. The structure factor  $S(k)$ , *cf.* Eq. (4), provides structural information on the long-ranged ordering of the system. Defined above,  $\varepsilon$  is a scaled potential energy and  $\eta$  is a metric for the extent of stealthiness. In addition, we use the small- $k$  features of  $S(k)$  to compare the extent of hyperuniformity between structures. Hyperuniform systems have the feature that  $S(k)$  vanishes as  $k$  approaches zero. We fit the small- $k$  regime (*i.e.*  $k < 0.5$ ) to a log-polynomial equation

$$\log S(k) = C_0 + C_1k + C_2k^2 + C_3k^3. \quad (13)$$

The parameter  $C_0$  can be considered to be a metric for the extent of hyperuniformity, where a

value that diverges to  $-\infty$  indicates that a system is hyperuniform. This metric is best used for relative comparisons among systems since numerical precision is limited. For example, one could say system A is more hyperuniform than system B because it has a lower value of  $C_0$ . However,  $C_0$  is not be a sufficient test to determine if a configuration is absolutely hyperuniform (*i.e.*, one should refrain from saying system A is absolutely hyperuniform).

We also employ the bond-order parameter  $\Psi_6$  defined as

$$\Psi_6 = \left| \frac{1}{N_{bonds}} \sum_j \sum_k e^{6i\theta_{jk}} \right| \quad (14)$$

where  $\theta_{ij}$  is the angle between two particles with respect to a fixed, but arbitrary, coordinate axis, to quantify the local orientation order. Particles are considered “bonded” if  $r_{ij} < 10$ , chosen so as to include nearest-neighbors. For the perfect triangular lattice,  $\Psi_6$  has a value of unity while for the ideal gas  $\Psi_6$  vanishes. Wavy crystals have value of  $\Psi_6$  that can range from about 0.4 to 0.8.

We introduce a configurational proximity parameter  $p$  defined as

$$p = \frac{\left( \sum_{i=1}^N |\mathbf{r}_{o,i} - \mathbf{r}_{f,i}|^2 \right)^{1/2}}{r_{NN}}, \quad (15)$$

where  $\mathbf{r}_{o,i}$  and  $\mathbf{r}_{f,i}$  are the positions of the RSA configuration and ground state configuration respectively and  $r_{NN}$  is the mean-nearest-neighbor in the RSA configuration. This metric  $p$  quantifies the closeness of two different particle configurations. In what follows, we will apply it to characterize the relative particle displacements required for a configuration to relax to the ground-state energy.

#### IV. RESULTS: COOLING AND QUENCHING

Before discussing the results of the quenching and cooling simulations, we briefly discuss some aspects of system-size effects related to the inherent structures of this system. While we previously showed that system-size effects were negligible when characterizing the ground states<sup>3</sup> and the equilibrium properties,<sup>2</sup> we find that there are appreciable system-size effects when considering the inherent structures and energy landscape.

We have compared inherent structures consisting 418 particles to 2340 particles sampled from the same temperature. In general, larger systems provide a slightly deeper quenching

of the potential energy. In addition, the bond-order parameters for larger systems tend to be less than that of smaller systems. This is expected since larger systems often have various polycrystalline-like domains that impart destructive interference on  $\Psi_6$ . The fraction of quenches from a fixed temperature that achieve the ground state varied considerably across system sizes. While the quenching of the energy of small systems occasionally resulted in achieving a ground-state structure, quenches of the large systems never resulted in a ground-state structure. The measure of the ground-state manifold becomes increasingly small as the system size increases. Given that the number of inherent structures increases exponentially with respect to system size,<sup>44</sup> it is unsurprising that larger systems would not sample the capture basins for ground states as frequently as smaller systems. System-size effects have been also been identified in the binary Lennard-Jones system.<sup>25</sup> Due to the system-size effects, we should not extrapolate true dynamical information from our results. Here, we present the analysis for 418-particle systems, noting that the trends across  $\chi$  values are similar to those in the 2340-particle system.

The properties of the excited-state (or thermalized) structures behave as expected. The thermodynamic properties lagged the equilibrium values as the system was cooled, and for slower cooling rates, the lag in thermodynamic properties was smaller than that for fast cooling rates. However, we find that the rate at which the system was cooled provided no distinguishable effects on the properties of the inherent structures when compared across various cooling rates. This should be contrasted with conventional glass-forming systems such as binary Lennard-Jones where systems cooled under slow rates found deeper wells in the energy landscape than systems cooled under faster rates.<sup>18</sup>

In our previous research, we have identified the approximate range for transitions from crystalline or wavy-crystalline to liquids to be in the temperature range of  $T^* < 0.00075$ .<sup>2</sup> We find that the temperature at which the inherent structures were sampled from had no distinguishable effect on the thermodynamics properties or structures. As the system was cooled, the systems hopped across various capture basins without regard to temperature.

Figure 3 exhibits the dynamics of systems as they sample inherent structures for  $\chi=0.6004$  and 0.8086 for 418 particles cooled at a rate of  $\gamma=10^{-7}$ . The figure shows the potential energy of inherent structures sampled every 30 time steps. In the figure, there are two classes of behaviors. For  $\chi = 0.6004$ , the system samples higher-energy inherent structures and also frequently samples ground states, those systems with  $\varepsilon < 10^{-10}$ . For  $\chi = 0.8086$ , the system

samples mostly higher-energy structures and occasionally, though far less frequently than for smaller  $\chi$ , samples ground states. For both values of  $\chi$ , the system hops to a new inherent structure between samplings. There were no consecutive samples that were identical except for very low temperatures far below the melting point (*e.g.*,  $T^* = 0.00015$ ). The rate at which the system samples capture basins does not appear to slow down significantly when the temperature is reduced as one might expect. This phenomenon occurred for all cooling rates we tested. In addition, even when sampling inherent structures every three time steps, the system never remained in the same basin for consecutive samplings. Note that the depths of the quenches for ground-state structures were deeper for  $\chi = 0.8086$  than for  $\chi = 0.6004$ . This demonstrates the issue that arises with finite-precision computing because these scaled energies should vanish to zero in a mathematical sense. In a practical sense, systems with energies below this threshold and orders of magnitude below the clusters of systems higher up are ground states.

We find that the structural features of the inherent structures did not vary with temperature either. Figure 4 shows the structure factor for inherent structures with  $\chi = 0.6004$  ensemble-averaged for several temperatures. However, when observing the structure factors for individual configurations, there is some small variability in the shape of  $S(k)$ . However, there are no clear correlations with temperature. In the figure, the structure factors associated with each temperature overlay nearly perfectly. Even at very low temperatures ( $T^* = 0.00015$ ), the structure factor for the inherent structures does not differ from those obtained from a liquid state.

For familiar systems, as the temperature is reduced, the potential energy of the inherent structures typically becomes lower as the system continues to reduce the potential energy through structural rearrangements, sampling deeper and deeper basins. However, we find as the temperature is reduced, the energy of the inherent structures does not appear to decrease. This reveals that the energy landscape is relatively flat and insensitive to temperature. The heights of the barriers, which we explore in Sec. VI, are therefore expected to be relatively small.

In Fig. 5, we plot the frequency in which the cooling and quenching procedure yielded a ground state for 418 particles. The plot shows the fraction of inherent structures that were ground states as a function of  $\chi$  for 3000 inherent structures for each  $\chi$ . We have found that the temperature from which the inherent structures are sampled does not have a significant



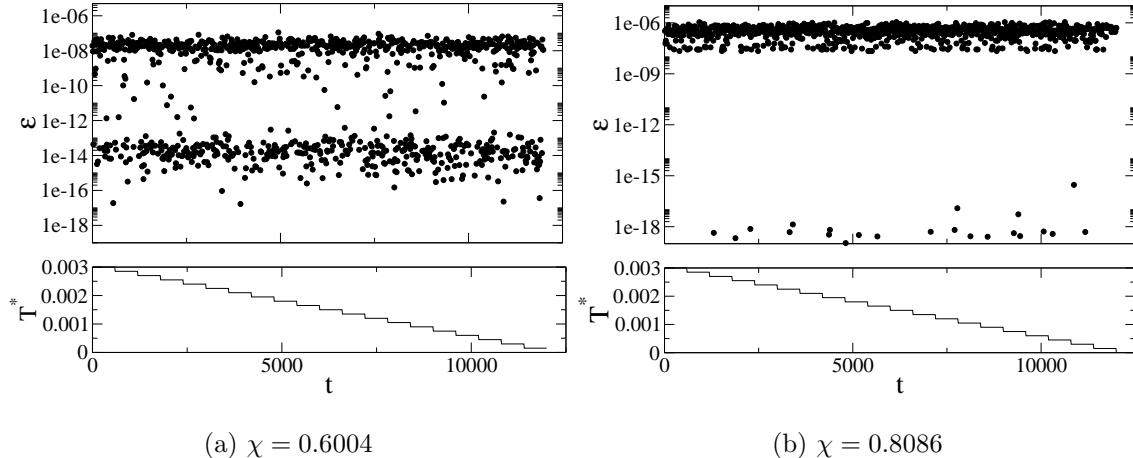


FIG. 3: Scaled potential energy  $\varepsilon$  of inherent structures as a function of time for  $\chi=0.6004$  and  $0.8086$ . The lower plots show the temperature schedules as a function of time. The temperature was reduced in a piecewise linear manner with an effective cooling rate of  $\gamma = 10^{-7}$ . Inherent structures were sampled every 30 time steps. As a function of time, the systems continually hop from one capture basin to another since no two consecutively-sampled structures have identical energies. We found that the effective cooling rate did not have a significant effect on the fluctuations of the energies of inherent structures. At low temperatures, systems evidently are not trapped in deep energy wells. For  $\chi = 0.6004$ , a significant fraction of inherent structures have an energy below the ground-state threshold of  $\varepsilon < 10^{-10}$ , while only a few inherent structures lie below this threshold for  $\chi = 0.8086$ .

effect on the rate at which the ground state is achieved. However, the value of  $\chi$  affects the frequency at which the ground state is found. In general, as  $\chi$  is increased from 0.6 to 0.9, the rate at which the ground states are found is reduced. However, for the “disordered-ground-state” region,  $\chi < 0.58$ , ground states were found infrequently. For example, in Fig. 5, the frequency in which ground states are found for  $\chi = 0.5622$  is much smaller than that of  $\chi = 0.6004$ . This suggests that the relative availability of the ground-state manifold is small for  $\chi < 0.58$ , becomes larger in the wavy-crystalline region ( $\chi > 0.58$ ), and then diminishes as the terminal  $\chi$  of 0.9 is reached. This shows that changes in  $\chi$  (and equivalently, density for fixed  $K$ ), fundamentally affect the shape and size of the ground state manifolds. An expansion or compression of the system does not simply rescale the energy landscape while maintaining its overall shape. Systems containing 2340 particles never achieved ground state energies, presumably because of the exponential growth in the number of inherent structures

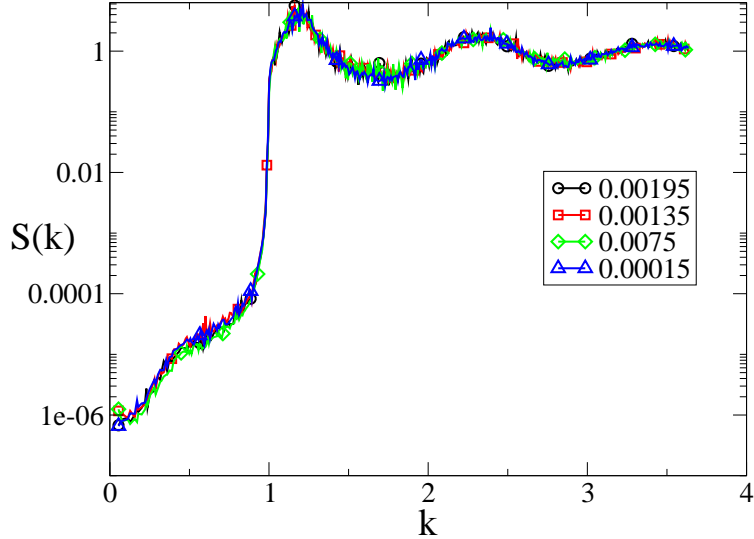


FIG. 4: (Color online) Structure factor for inherent structures with  $\chi=0.6004$  and  $N=418$  and at various dimensionless temperatures  $T^*$  - 0.00195 (circles), 0.00135 (squares), 0.0075 (diamonds), and 0.00015 (triangles). Each temperature is ensemble averaged over 50 configurations sampled from a molecular dynamics trajectory. Despite the range of temperatures, temperature has little effect on the inherent structures.

with system size.<sup>44</sup>

## V. RESULTS: STRUCTURAL CHARACTERISTICS

Figures 6 and 7 show inherent structures obtained via the cooling and quenching procedure. These structures display features that are common among inherent structures. Upon examining the inherent structures, we found several structural motifs - five-particle rings, wavy grain boundaries, and vacancy-interstitial defects. The frequency of these features varies depending on  $\chi$ . For  $0.5 < \chi < 0.6$ , the five-particle ring, as demonstrated in Fig. 6, is the most prevalent feature. The five-particle ring arises due to the local interactions of constituent particles. The nearest- and second-nearest neighbor distances lie within the first and second wells of  $v(r)$  respectively. The ratio of the relative distances creates a frustration that favors the local five-particle ring. Evidently, these local forces are more dominant than the long-range forces that promote stealthiness.

For  $0.58 < \chi < 0.89$ , a common feature of inherent structures is a wavy grain boundary as evident in Figs. 6 and 7. In these images, the grain boundaries manifest themselves in a

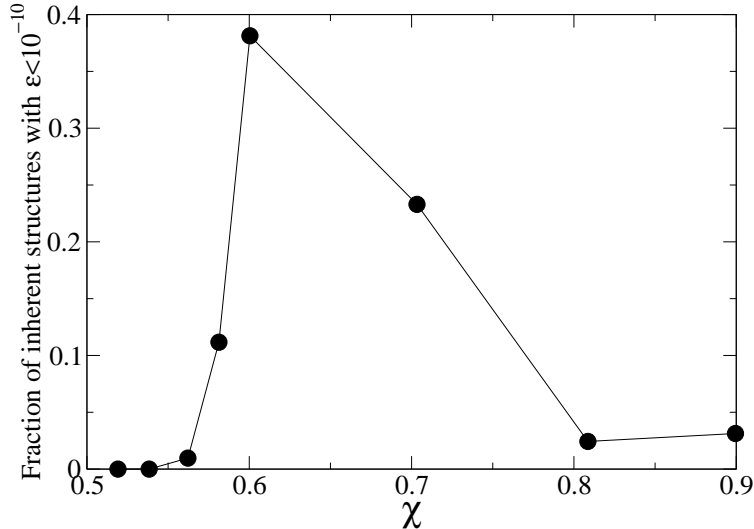


FIG. 5: Fraction of inherent structures obtained via the cooling and quenching procedure with  $\gamma = 10^{-8}$  and  $N = 418$  that are ground states (*i.e.*, scaled potential energy  $\epsilon < 10^{-10}$ ). Data represent the average of four independent cooling runs with 750 samples for each run.  $\chi$  values of 0.6004 and 0.7033 achieved the highest fraction of ground states.

more wavy form than one might see in a Lennard-Jones inherent structure, in which particles prefer to align in straight lines. This  $\chi$  range is associated with wavy-crystalline ground states, which appear as a uniformly sheared triangular or square lattice. This behavior evidently manifests itself in the inherent structures where the grain boundaries appear to have some waviness. For these  $\chi$  values, the long-range nature of the potential is sufficiently strong to inhibit five-particle rings in favor of the wavy grains. Lastly, for  $\chi = 0.8995$ , the last image in Fig. 7, the inherent structures either have a large grain boundary of perfectly aligned particles, vacancy-interstitial pairs, or both. These inherent structures also exhibit polycrystallinity. In the cases of  $\chi > 0.58$ , the multiple wavy domains appear to be in structural conflict with each other. This is best demonstrated by Fig. 6 for  $\chi = 0.6004$  where several domains appear to meet in the middle of the system. This conflict evidently “jams” the system and prevents it from reaching the ground state.

Observing the structure factor for inherent structures shows that inherent structures with smaller  $\chi$  are more stealthy and more hyperuniform than those at higher  $\chi$ . However, inherent structures that are not ground states were neither completely stealthy nor hyperuniform. In Fig. 8, we show the ensemble-averaged  $S(k)$  for 50 inherent structures

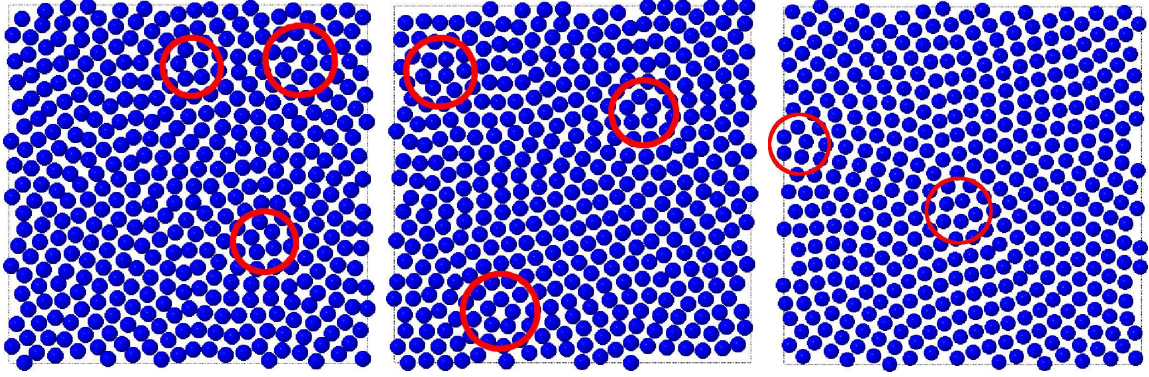


FIG. 6: (Color online) Inherent structures produced from the cooling and quenching procedure sampled from a high-temperature liquid ( $T^* = 0.0018$ ) for  $\chi = 0.5191$  (left),  $0.5622$  (middle), and  $0.6004$  (right) for 418 particles. These structures demonstrate the five-particle clusters that are common in inherent structures for these  $\chi$  values. The five-particle rings are highlighted by a surrounding circle. The buildup of wavy grains are visible for  $\chi = 0.6004$ .

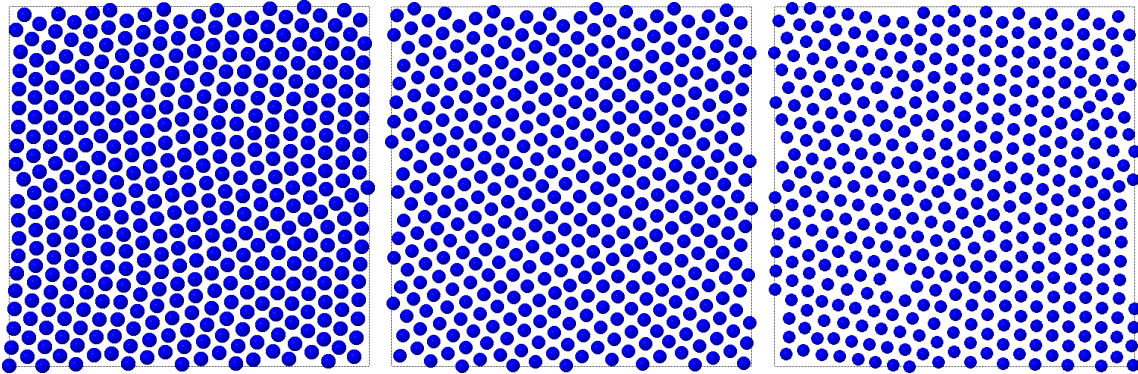


FIG. 7: (Color online) Inherent structures produced from the cooling and quenching procedure sampled from a high-temperature liquid ( $T^* = 0.0018$ ) for  $\chi = 0.7033$  (left),  $0.8086$  (middle), and  $0.8995$  (right) for 418 particles. These structures demonstrate the wavy grains and vacancy-interstitial defects common to inherent structures for  $\chi > 0.58$ . As  $\chi$  increases, the inherent structures are more ordered, though grain boundaries prevent the systems from minimizing the energy.

sampled at  $T^* = 0.00105$  for various  $\chi$ . For the smallest  $\chi$  value, the small- $k$  tail of the structure factor initially decreases and then rapidly increases as  $k$  is increased toward unity. The shape of the small- $k$  tail of  $S(k)$  remains constant but is shifted to higher values (less hyperuniform) as  $\chi$  increases to  $\chi = 0.5813$ .

However, as  $\chi$  leaves the disordered-ground-state regime, the shape of the curve changes, as exemplified by the curves for  $\chi=0.6004$  and  $0.7033$ . In Fig. 8, the curve for  $\chi = 0.6004$  demonstrates the new shape. For the small- $k$  region,  $S(k)$  initially has a negative slope which quickly turns positive, and nearly flattens before diverging near  $K$ . The shape of this ensemble-averaged  $S(k)$  is due to the relatively large number of ground states that arise in the inherent structure analysis for this  $\chi$ . For  $\chi = 0.6004$ , nearly 40% of inherent structures are ground states, and this  $S(k)$  represents the average of the ground-state  $S(k)$  and the inherent structure  $S(k)$ . A similarly large fraction of inherent structures are ground states for  $\chi=0.7033$ . If the ground states are removed from the ensemble-averaging, the structure factor appears more like those associated with  $\chi=0.8086$  and  $0.8995$ . For these  $\chi$ ,  $S(k)$  has a initial negative slope that turns positive near  $k=0.5$ , which then diverges near  $K$ .

It is interesting to note that the way in which systems get “stuck” in an inherent structure for  $\chi$  in the disordered regime is different than that of the wavy-crystalline regime. For  $\chi < 0.58$ , the systems struggle most to minimize  $S(k)$  for  $k > 0.5$ . The length scale associated with  $k > 0.5$  corresponds to local interactions in real space (*i.e.*, on the order of a few particle diameters). This manifests itself with the five-particle rings. For  $\chi > 0.58$ , the systems have difficulty minimizing  $S(k)$  near zero and unity. The  $k$ -values near zero represent longer-range interactions than the  $k$ -values near unity. The inherent structures for  $\chi > 0.58$  are therefore “stuck” on a longer length scale. It is no surprise then that the inherent structures appear locally ordered but are frustrated with a grain boundary.

It is obvious that as  $\chi$  increases the extent of hyperuniformity of the inherent structures diminishes. This is shown in an ensemble sense in Fig. 8. However, we have also shown this general relationship for individual structures. In Fig. 9, we display the hyperuniformity coefficient  $C_0$  for the log-polynomial fit to  $S(k)$  in Eq. (13). In the figure, each data point represents one inherent structure. There are two clusters of points, where the cluster of points on the lower left are typically ground states where  $S(k)$  vanishes as  $k$  approaches zero, but due to numerical precision the hyperuniformity coefficient  $C_0$  remains finite. In the cluster in the upper right of Fig. 9, there is a linear relation between  $C_0$  and  $\log \eta$ . Also, it is clear that as  $\chi$  increases, the hyperuniformity parameter  $C_0$  also increases. A few outlying structures are present for  $\chi=0.7003$ ,  $0.8086$  and  $0.8995$ . These structures appear as triangular lattices with very slight waves or shear applied to them, a sufficient amount that they are not ground states, but still have very small limiting values of  $S(k)$  as  $k$  approaches

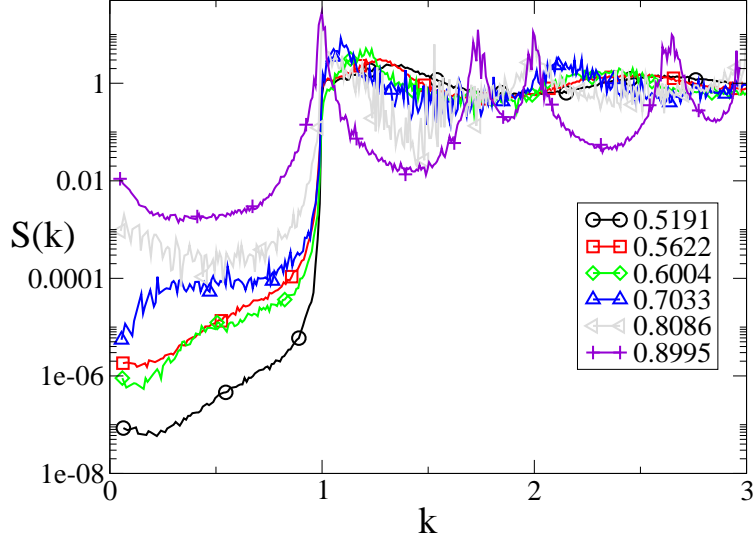


FIG. 8: (Color online) Structure factor for inherent structures as a function of  $\chi$  ensemble averaged over 50 configurations sampled from a molecular dynamics trajectory at  $T^* = 0.00105$  for a system of 418 particles. As  $\chi$  increases, the inherent structures become less stealthy. Also, the extent of hyperuniformity decreases when  $\chi$  is increased.

zero.

The stealthiness of the inherent structures, as characterized by the metric  $\eta$ , in general does not have a relation to the six-fold bond-order orientational order of a system. Figure 10 shows the bond-order parameter  $\Psi_6$  as a function of stealthiness  $\eta$  for various inherent structures. For each  $\chi$  value, there is a range of available  $\eta$  and  $\Psi_6$ . Initially, for  $\chi$  near 0.5, these ranges are rather narrow, and as  $\chi$  increases, these ranges become much broader. For large  $\chi=0.8086$  there is a large diversity of  $\Psi_6$  and  $\eta$  available for inherent structures. However, for  $\chi=0.8995$ , there is a narrow band of available  $\eta$  but a large range of  $\Psi_6$  depending on the number and orientation of opposing crystalline domains. The group of structures for  $\chi=0.8995$  and  $\eta \sim 0.02$  are those structures with only vacancy-interstitial defects.

The bond-order parameter also shows considerable variation when plotted against the hyperuniformity parameter  $C_0$ . Figure 11 shows  $C_0$  as a function of  $\Psi_6$  for various  $\chi$  values. As  $\chi$  increases, the variation in  $\Psi_6$  grows while  $C_0$  generally falls into a narrow range of values. This figure demonstrates that hyperuniformity does not necessarily require local six-fold ordering. Systems with  $\chi=0.7033$  have the largest range of available local six-fold

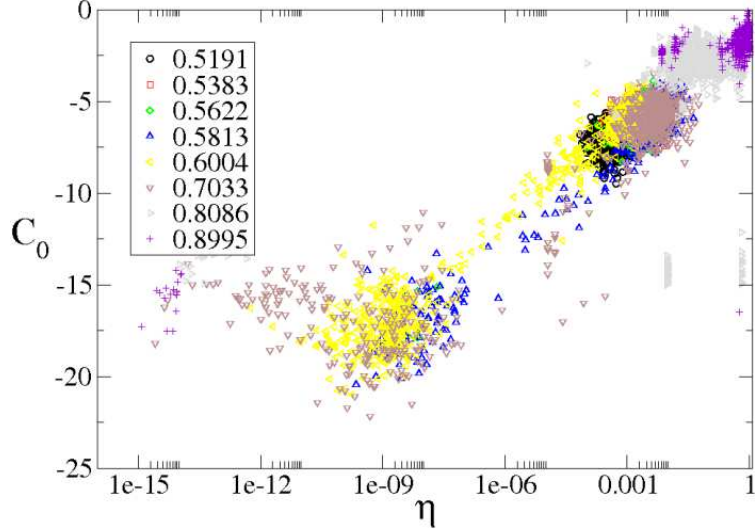


FIG. 9: (Color online) Hyperuniformity parameter  $C_0$  versus stealthiness metric  $\eta$  for inherent structures generated from the MD and quench procedure. There is a clear relation between the hyperuniformity coefficient  $C_0$  and the stealthiness metric  $\eta$ , although there exist outlying configurations. There is also a positive relation between  $C_0$  and  $\chi$ . Those configurations in the lower left with  $\eta < 10^{-9}$  are typically ground states. 800 configurations are shown for each  $\chi$  value.

ordering for more hyperuniform structures because  $\Psi_6$  ranges from as low as 0.1 to just below unity.

## VI. PATHS FROM INHERENT STRUCTURES TO GROUND STATES

The nudged-elastic-band algorithm was used to determine the minimum-energy path from a ground-state structure to an inherent structure nearby in configurational space. We find that the height of the barrier between the ground state and the inherent structure generally increases with  $\chi$ . However, there are instances that deviate from this general situation. Figure 12 illustrates the minimum-energy paths found for various  $\chi$  from the ground state (point zero on the reaction pathway) to the inherent structure (last point on the reaction pathway). The pathway is discretized over fifty images. In all the cases, the landscape is locally quadratic near the ground state and inherent structure. The maximum for each pathway represents the saddle point in the energy landscape separating the ground state and inherent structures. Connections from the triangular lattice to inherent structures were challenging to construct because of the zero-energy modes present in triangular-lattice



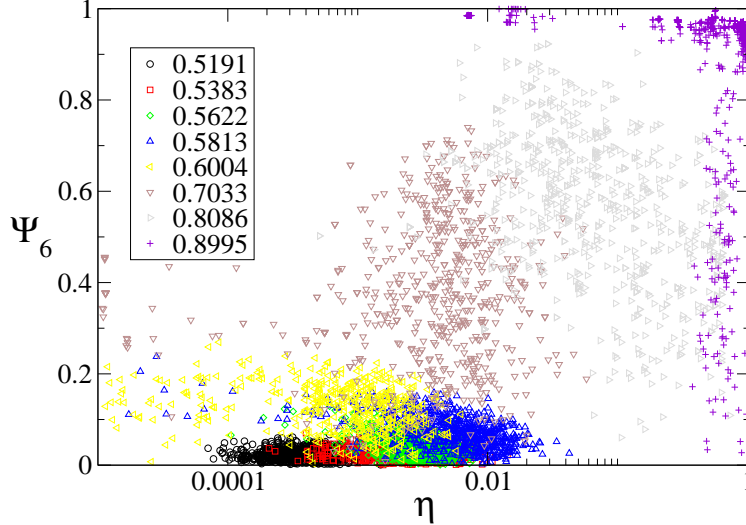


FIG. 10: (Color online) Bond-order parameter  $\Psi_6$  versus stealthiness metric  $\eta$  for inherent structures generated from the MD and quench procedure. As  $\chi$  increases, there is an increasing degree of six-fold ordering. However, for large  $\chi$ , the range of available  $\Psi_6$  extends larger due to the polycrystalline nature of the configurations. 800 configurations are shown for each  $\chi$  value. For clarity, we omit those structures with  $\eta < 10^{-5}$  so that the plot can provide more detail about the inherent structures.

systems. The nudged-elastic-band algorithm encountered difficulty in traversing through zero-energy valley and then uphill toward a saddle point. In all cases except  $\chi=0.8995$ , we report transitions from non-lattice ground states to inherent structures.

For  $\chi < 0.6$  (left in Fig. 12), the barrier height,  $\varepsilon_{sad}$  is significantly large compared to the difference in the energies of the ground-state and inherent structures (*i.e.*,  $\varepsilon_{inh} - \varepsilon_{gs} \ll \varepsilon_{sad}$ ). When  $\chi$  becomes larger, as in the case for  $\chi=0.7033$  and higher, middle and right in Fig. 12,  $\varepsilon_{sad}$  is nearly equivalent in height. For the case of  $\chi=0.8995$ , the minimum-energy path appears to flatten out as it approaches the inherent structure. In reality, there is a maximum energy along the path, although it is difficult to discern due to the scaling in the plot. In the cases where the energy of the inherent structure is nearly equal to the barrier height, small perturbations from the inherent structure can allow the system to relax to the ground state. On the other hand, for smaller  $\chi$ , relatively higher-energy perturbations are necessary for the inherent structure to climb the energy barrier and fall to the ground state. While there are exceptions to this phenomenon, they usually occur when the inherent structure and ground state are not nearby in the energy landscape (*i.e.*, there is a another inherent



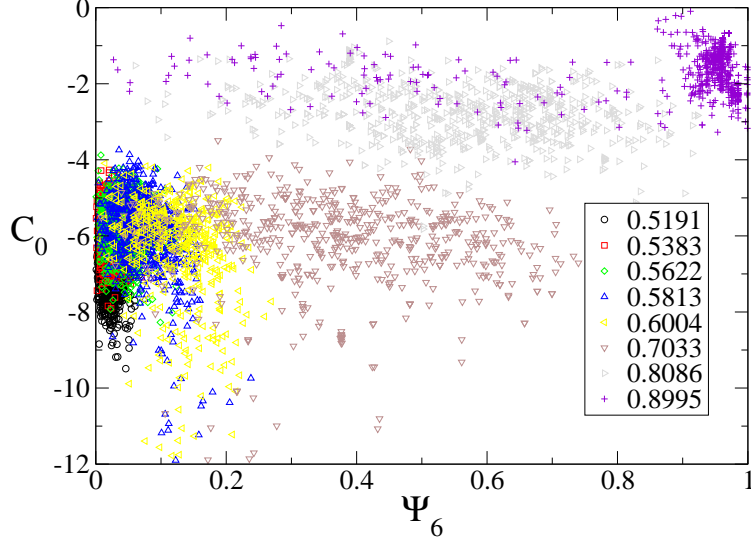


FIG. 11: (Color online) Hyperuniformity parameter  $C_0$  versus bond-order parameter  $\Psi_6$  for inherent structures generated from the MD and quench procedure. Despite the broad range of six-fold ordering at larger  $\chi$ , the level of hyperuniformity remains consistent across  $\chi$  values. 800 configurations are shown for each  $\chi$  value. For clarity, we omit those structures with  $C_0 < -12$  so that the plot can provide more detail on the inherent structures.

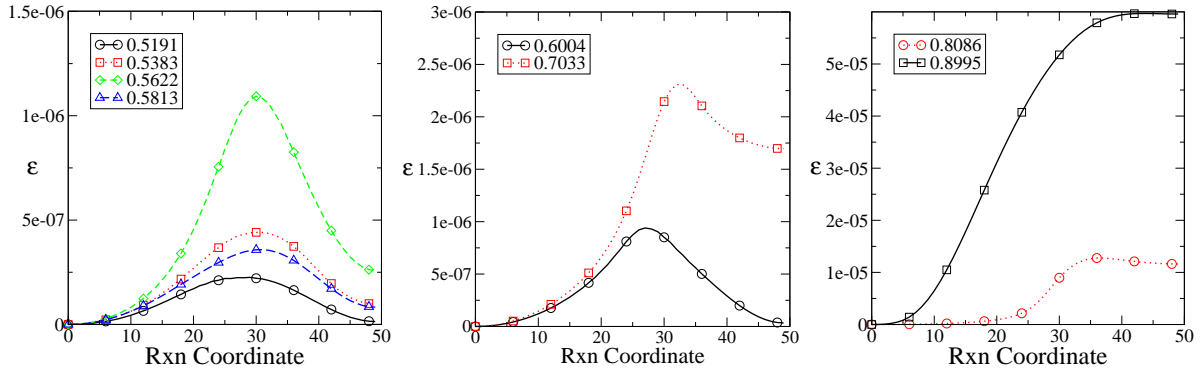


FIG. 12: (Color online) Representative minimum-energy paths from ground states (point zero on the reaction coordinate) to inherent structures (last point on the reaction coordinate) along a generalized reaction pathway for  $N = 418$  for (a)  $0.5 < \chi < 0.6$ , (b)  $\chi = 0.6004$  and  $0.7033$ , and (c)  $\chi = 0.8086$  and  $0.8995$ . The local maximum corresponds to a saddle point in the energy landscape.

structure closer to the ground state). Along these paths, the configurational proximity metric  $p$  monotonically decreases along the path from the ground state to the inherent structure. The metric  $p/N$  for the proximity per particle between the inherent structure

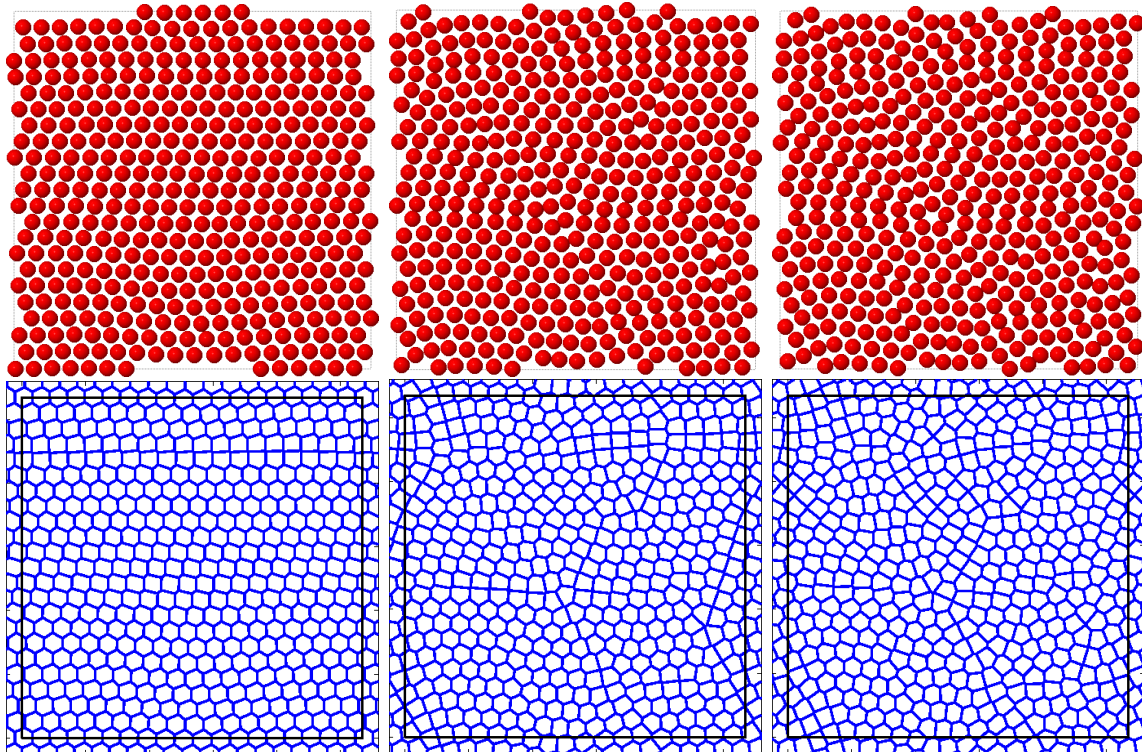


FIG. 13: (Color online) Configurations (top row) and associated Voronoi tessellations (bottom row) for the minimum-energy path from ground state (left column) through the saddle point (middle column) to the inherent structure (right column) for  $\chi = 0.5383$ . The transitions are from the set described in Fig. 12.

and the ground state is of the order 0.1. On average, particles are collectively displaced by 10% of the nearest neighbor spacing to achieve a ground state.

In Figs. 13 and 14, we display the ground state, saddle point, and inherent structure and the associated Voronoi diagrams for  $\chi=0.5383$  and  $0.7033$ . These are the same paths shown in Fig. 12. These systems are representative of the types of local rearrangements found in the transition from ground states to inherent structures. In Fig. 13, the ground state has wavy-crystalline characteristics where there is alignment in one direction. The Voronoi diagram appears to have highly ordered arrangement of polygons. In the saddle point images, one can see the appearance of the five-particle rings. In the inherent structure, the defect appears to be localized, however, the defects are more easily discerned in the Voronoi diagram.

For  $\chi=0.7033$ , the buildup of the grain boundary is clear in Fig. 14. The ground state is wavy-crystalline and the saddle point shows the appearance of a vertical and horizontal

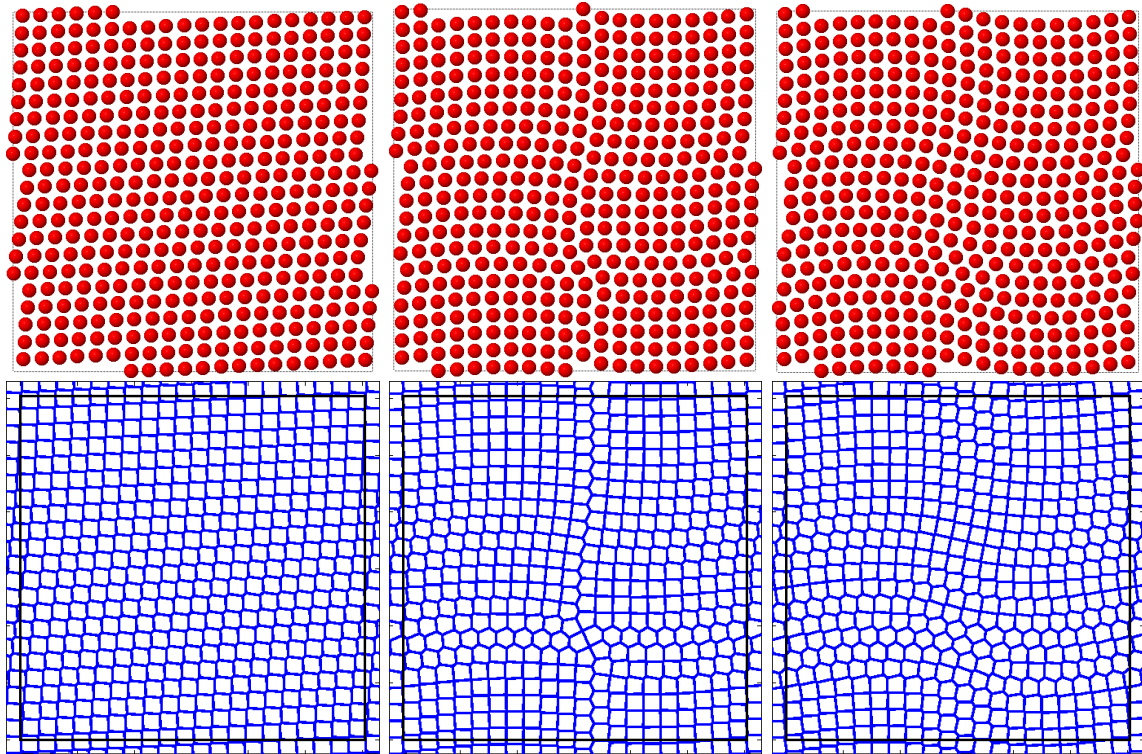


FIG. 14: (Color online) Configurations (top row) and associated Voronoi tessellations (bottom row) for the minimum-energy path from ground state (left column) through the saddle point (middle column) to the inherent structure (right column) for  $\chi = 0.7033$ . The transitions are from the set described in Fig. 12.

grain. The inherent structure shows the apparent mismatch between lines of particles that is responsible for the inability to reach the ground state. The Voronoi diagrams in this case visually display the source of the frustration in the system. While far from the grain, the polygons in the Voronoi diagram for the inherent structure are quite regular and ordered, those near the grain boundary have much more variation in shape. For  $\chi=0.8995$ , the rearrangements found in the transition from a perfect lattice to one with a vacancy-interstitial pair are very local (albeit collective), only involving the few particles immediately surround the interstitial-vacancy pair. In all cases observed, the rearrangements from ground states to inherent structures involve only local, but collective, rearrangements (within a few particle diameters). As highlighted here, they typically involve the formation of a grain boundary or a five-particle ring.

## VII. PARTICLE REARRANGEMENTS FROM RSA PATTERNS TO GROUND STATES

Configurations generated by random sequential addition near the saturation densities are known to suppress long-wavelength scattering, described as “ultratransparent,”<sup>35,36</sup> though images of the structure factor for the RSA configuration demonstrates that it is not hyperuniform and not absolutely stealthy.<sup>37</sup> From Ref. [34], as  $k$  approaches zero, the structure factor approaches a value of 0.059, corresponding to a value of the hyperuniformity parameter  $C_0$  of -1.23.

In Figs. 15 and 16, we display the initial RSA configurations and the final ground-state configurations as obtained from the collective coordinate approach, for  $\chi$  values of 0.0991 and 0.3657. Each figure also displays the corresponding Voronoi tessellation derived from the point patterns. In both cases when observing the dynamics of the minimization algorithm, one observes a general spreading of particles due to the repulsion for small  $r$ . These collective rearrangements are very local and there are no large global rearrangements involved. While every particle is displaced collectively from their initial location, each particle is displaced by a small fraction of the mean-nearest neighbor distance, as measured by the proximity metric per particle,  $p/N$ .

In Fig. 15, one can observe similar arrangements of particles in both the RSA configuration and the ground-state configuration. These images would be difficult to distinguish visually. Several structural features remain in tact aside from the general spreading of particles. In the Voronoi tessellations of the RSA configuration, there are areas where the local density appears higher than in other areas. However, in the tessellation of the ground state, these areas of higher local density have been relaxed away. The density appears much more uniform in the ground state than the RSA configuration. However, the visual difference between the two images are subtle. In Fig. 16, the spreading remains local, although it is clear that the repulsion is stronger. The particles, on average, travel a larger distance and fewer structural features of the RSA pattern are maintained. The Voronoi tessellation of the ground state appears to have more uniform cell sizes than the RSA configuration, though the differences are subtle.

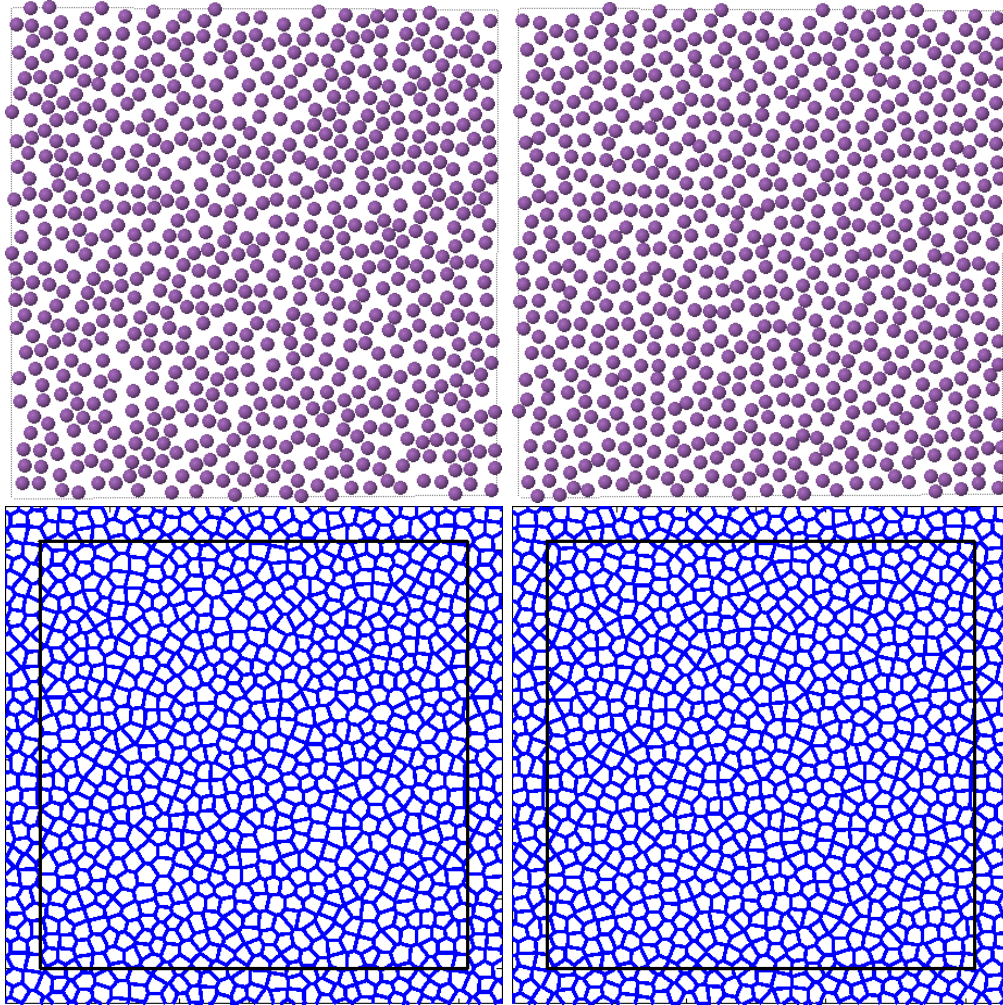


FIG. 15: (Color online) (Top) Configurations with  $\rho = 0.1953$  and  $\chi = 0.0991$  and (bottom) the associated Voronoi diagrams. The left images are the initial RSA configurations and the right images are the ground states. The trajectory from the RSA configuration to the ground state appears to arise from a gentle repulsion. The diameters of the particles correspond roughly to the assigned RSA diameter. The dark lines represent the system box.



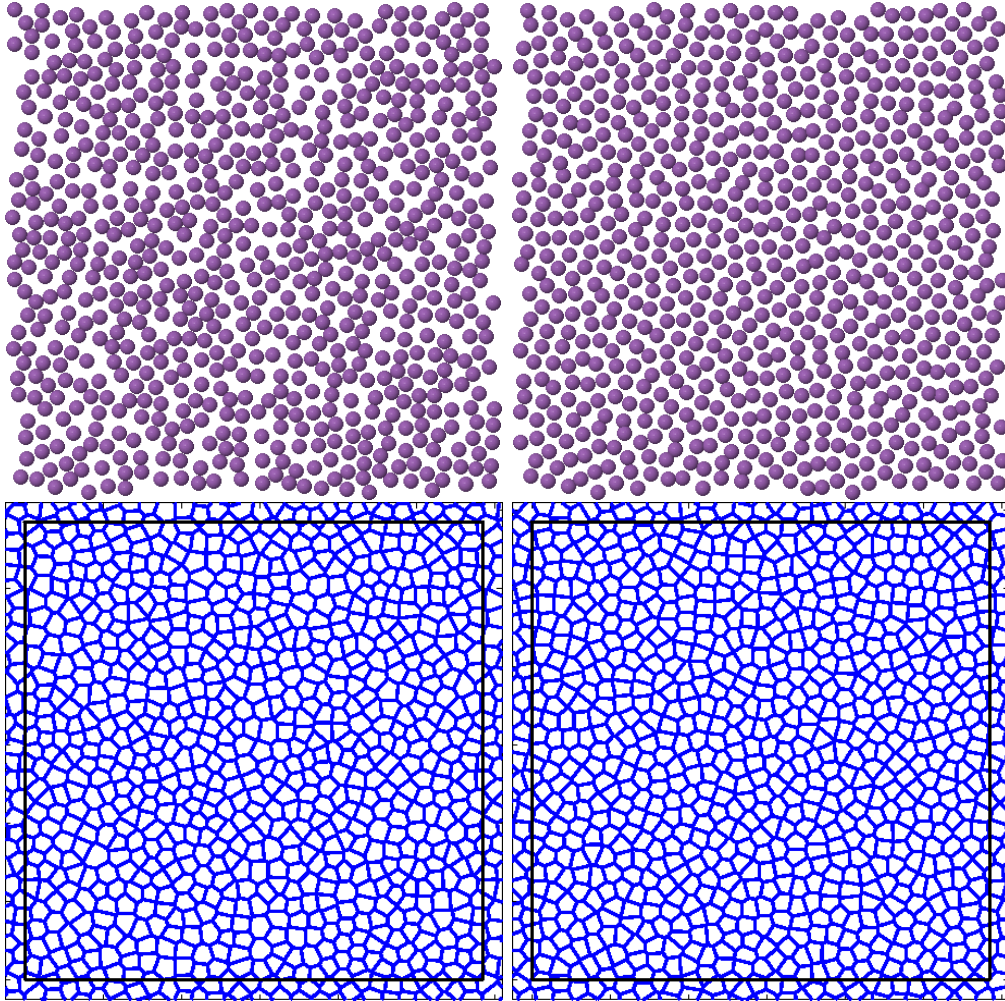


FIG. 16: (Color online) (Top) Configurations with  $\rho = 0.05434$  and  $\chi = 0.3657$  and (bottom) the associated Voronoi diagrams. The left images are the initial RSA configurations and the right images are the ground states. The trajectory from the RSA configuration to the ground state appears to arise from a gentle repulsion. The diameters of the particles correspond roughly to the assigned RSA diameter. The dark lines represent the system box.

TABLE I: Comparison of RSA configurations to their associated ground states.

$\rho$	$\chi$	$N$	$D$	$\phi_{rsa} - \phi_{gs}$	$\eta_{rsa}$	$p$	$p/N$
0.19973	0.0974	749	1.866	$5.928525 \times 10^4$	0.06614	4.653	0.00621
0.19653	0.0991	737	1.883	$5.462281 \times 10^4$	0.05879	5.258	0.00713
0.14660	0.1364	733	2.155	$5.962653 \times 10^4$	0.07407	4.915	0.00671
0.09893	0.1995	742	2.639	$6.560097 \times 10^4$	0.07569	6.354	0.00856
0.06851	0.2902	734	3.154	$7.001039 \times 10^4$	0.08924	6.535	0.00890
0.05434	0.3657	741	3.559	$7.501234 \times 10^4$	0.09812	6.943	0.00937
0.04678	0.4227	731	3.809	$8.202199 \times 10^4$	0.11910	8.342	0.01141
0.04161	0.4818	743	4.072	$8.081648 \times 10^4$	0.14692	10.99	0.01478

We have quantified the differences between the RSA structures and the ground states for several RSA configurations at various  $\chi$  values. Table I displays the parameters of these systems as well as the differences in potential energy  $\phi$  between the RSA system and ground state, the stealthiness metric for RSA configurations  $\eta_{rsa}$ , and the configurational proximity metric  $p$ . The stealthiness metric  $\eta$  for ground states vanishes identically to zero.

There are some variations in energies and metrics that are attributed to finite system size. Structural features of the RSA patterns can vary across samples, and these variations show up in Table I particularly for small  $\chi$ . In general, the difference between the potential energy of the RSA system and the ground state increases uniformly with  $\chi$ , but is on the order of  $10^{-4}$ . The stealthiness metric also increases uniformly with  $\chi$  as is expected, since decreasing the density of RSA configurations will rescale the structure factor to be less stealthy. The configurational proximity metric  $p$  increases uniformly with  $\chi$ , ranging on a per particle basis of 0.00621 to 0.01478 for these  $\chi$ . These metrics show that particles in the RSA configuration need to be collectively displaced locally by a small fraction of the mean-nearest-neighbor distance in order to produce stealthy, hyperuniform systems.

## VIII. DISCUSSION

In this paper, we have shown that the energy landscape associated with the  $k$ -space overlap potential is relatively flat and devoid of deep energy wells. This is to be contrasted

with Lennard-Jones systems, which possess rugged energy landscapes. The sampling of inherent structures from the energy landscape is independent of the temperature from which the system was sampled and the rate at which the system was cooled. Five-particle rings, which are related to the local interactions between particles, disrupt the ability of a system to become a stealthy ground state, while grain boundaries, which arise for  $\chi$  values in the wavy-crystalline regime, are attributed to the longer-range interactions in a system. While the hyperuniformity parameter  $C_0$  and the stealthiness parameter  $\eta$  are positively correlated with each other, the bond-order parameter  $\Psi_6$  can display a broad range of characteristics for various  $\chi$  values. We have used the nudged-elastic-band algorithm to show that local particle rearrangements can allow systems to be perturbed over a relatively small energy barrier from an inherent structure to a ground state. These rearrangements correspond to a low configurational proximity metric  $p$ . Lastly, we have shown that highly local collective particle displacements, as quantified via the configurational proximity metric  $p$ , are sufficient to convert a RSA configuration into a stealthy, hyperuniform ground state.

While these studies represent another contribution to understanding the nature of these unusual long-ranged potentials, there are some natural extensions to this work that can further illuminate the relationship between particle interactions, stealthiness, and hyperuniformity. We have used simple metrics  $C_0$  and  $\eta$  as measures of stealthiness and hyperuniformity, there are a multitude of other metrics that can be constructed. Measuring hyperuniformity for a single finite system is challenging due to the fluctuations and noise that can arise in the small- $k$  behavior of  $S(k)$ . Ideally, one would prefer to have a large system where the number variance in an observation window can be measured accurately. However, we are limited in system size because of numerical methods. While our measurement of stealthiness is directly related to the structure factor, we assumed equal weights for all the  $S(k)$ , while one could assign weights differently to favor small- $k$  scattering or near- $K$  scattering. Currently, there are no obvious metrics that stand out as superior to those used here. However, the development of new, improved metrics remains a potential direction of future research.

While our paths connect ground states to inherent structures, a more generic algorithm taking inherent structures to ground states would be valuable. For instance, our methods relied on knowledge of the ground state and inherent structure *a priori*. However, a more useful method would be to find the nearest ground-state structure given only an inherent structure. This algorithm would be far more powerful than the current method. One could



further quantify the possible rearrangements in the inherent structures in order to help produce such an algorithm that relies on trial displacements that search for small energy barriers nearby. This could lead to a statistical analysis of the types of rearrangements made in a system to determine which are more likely to lead to a ground state. In addition, a more in-depth study of the rearrangements from RSA configurations to hyperuniform and stealthy configurations would be meaningful. Perhaps one can distinguish the relative contributions of the features of the interaction potential that contribute to the hyperuniformity and stealthiness of a system.

The precise role of the pair interactions in the formation of disordered ground states and stealthiness is unknown. Here, we have determined that five-particle rings are a consequence of the first two minima in the overlap potential  $v(r)$ . The ground-state behavior holds for a class of potentials<sup>3</sup> and we strongly suspect that similar behavior in the inherent structure analysis may generally hold as well. A systematic study involving the determination of ground states for the truncated overlap potential in Eq. (7) might help understand how many local minima in  $v(r)$  are necessary for disordered ground states to arise. The potential could be truncated at the first, second, third, *etc.* minimum and numerical procedures could be used to find ground-state structures. This would encounter issues of rigor in that the structures found by numerical methods may not touch the lower bound on  $\phi$ . The trivial lower bound for  $\phi$  is zero (due to the nonnegativity of the overlap potential), but for the densities associated with the disordered and wavy-crystalline regimes, the improved lower bound, that being  $S(k)$  must vanish for all  $k < K$ , is not applicable to the truncated  $k$ -space overlap potential.

In addition, we observed that the shape of  $V(k)$ , which assigns weights to  $S(k)$  in the potential-energy function, apparently influences the shape of the function  $S(k)$  for the inherent structures for  $\chi < 0.58$ . Above this  $\chi$  value, there was no obvious connection between  $V(k)$  and  $S(k)$  for the inherent structures. This raises the question as to whether the shape of  $V(k)$  actually influences the shape of the function  $S(k)$  for inherent structures. A simple study varying the shape of  $V(k)$ , but maintaining the compact support at  $K$  and the positivity of  $V(k)$  would help answer this question.

Lastly, while this collective coordinate setup was used understand and design new materials in two-dimensions, such as photonic bandgap materials,<sup>13</sup> the extension to three dimensions should be particularly fruitful. While we have some understanding of stealthy

ground states in three dimensions,<sup>3,4</sup> the relations between inherent structures and ground states may be different in three dimensions than two dimensions. Connecting these structural rearrangements and physical properties can help to contribute to the next class of three-dimensional photonic bandgap materials.

### **Acknowledgments**

This research was supported by the U.S. Department of Energy, Office of Basic Energy Sciences, Division of Materials Sciences and Engineering under Award DE-FG02-04-ER46108.

- 
- \* Corresponding author; Electronic address: torquato@electron.princeton.edu
- <sup>1</sup> R. D. Batten, F. H. Stillinger, and S. Torquato, Phys. Rev. Lett **103**, 50602 (2009).
  - <sup>2</sup> R. D. Batten, F. H. Stillinger, and S. Torquato, Phys. Rev. E **80**, 31105 (2009).
  - <sup>3</sup> R. D. Batten, F. H. Stillinger, and S. Torquato, J. Appl. Phys. **104**, 033504 (2008).
  - <sup>4</sup> O. U. Uche, S. Torquato, and F. H. Stillinger, Phys. Rev. E **74**, 31104 (2006).
  - <sup>5</sup> S. Torquato and F. H. Stillinger, Phys. Rev. Lett. **100**, 020602 (2008).
  - <sup>6</sup> S. Torquato, Soft Matter **5**, 1157 (2009).
  - <sup>7</sup> Y. Fan, J. K. Percus, D. K. Stillinger, and F. H. Stillinger, Phys. Rev. A **44**, 2394 (1991).
  - <sup>8</sup> O. U. Uche, F. H. Stillinger, and S. Torquato, Phys. Rev. E **70**, 46122 (2004).
  - <sup>9</sup> C. E. Zachary and S. Torquato, Phys. Rev. E, in press, (2011).
  - <sup>10</sup> S. Torquato and F. H. Stillinger, Phys. Rev. E **68**, 41113 (2003).
  - <sup>11</sup> C. E. Zachary and S. Torquato, J. Stat. Mechanics: Theory and Exp., P12015, (2009).
  - <sup>12</sup> C. E. Zachary, Y. Jiao, and S. Torquato, Phys. Rev. Lett., in press, (2009).
  - <sup>13</sup> M. Florescu, S. Torquato, and P. Steinhardt, Proc. Nat. Acad. Sci. **106**, 20658 (2009).
  - <sup>14</sup> W. Man, M. Florescu, K. Matsuyama, P. Yadak, S. Torquato, P. J. Steinhardt, and P. Chaikin, in *Conference on Lasers and Electro-Optics* (Optical Society of America, 2010).
  - <sup>15</sup> P. G. Debenedetti, *Metastable liquids: concepts and principles* (Princeton University, 1996).
  - <sup>16</sup> M. Goldstein, J. Chem. Phys. **51**, 3728 (1969).
  - <sup>17</sup> P. G. Debenedetti and F. H. Stillinger, Nature **410**, 259 (2001).
  - <sup>18</sup> S. Sastry, P. G. Debenedetti, and F. H. Stillinger, Nature **393**, 554 (1998).
  - <sup>19</sup> F. H. Stillinger and T. A. Weber, Phys. Rev. A **28**, 2408 (1983).
  - <sup>20</sup> F. H. Stillinger and T. A. Weber, J. Chem. Phys. **81**, 5095 (1984).
  - <sup>21</sup> A. Heuer, Phys. Rev. Lett. **78**, 4051 (1997).
  - <sup>22</sup> F. H. Stillinger and T. A. Weber, J. Chem. Phys. **87**, 2833 (1983).
  - <sup>23</sup> T. A. Weber and F. H. Stillinger, Phys. Rev. B **31**, 1954 (1985).
  - <sup>24</sup> T. Weber and F. Stillinger, Phys. Rev. B **32**, 5402 (1985).
  - <sup>25</sup> S. Büchner and A. Heuer, Phys. Rev. E **60**, 6507 (1999).
  - <sup>26</sup> K. Broderix, K. K. Bhattacharya, A. Cavagna, A. Zippelius, and I. Giardina, Phys. Rev. Letters **85**, 5360 (2000).

- <sup>27</sup> C. Oligschleger and H. R. Schober, Phys. Rev. B **59**, 811 (1999).
- <sup>28</sup> E. La Nave, F. Sciortino, P. Tartaglia, M. S. Shell, and P. G. Debenedetti, Phys. Rev. E **68**, 32103 (2003).
- <sup>29</sup> C. Likos, Phys. Rep. **348**, 267 (2001).
- <sup>30</sup> N. W. Ashcroft and N. D. Mermin, *Solid State Physics* (Saunders College: Philadelphia, Pa, 1976).
- <sup>31</sup> S. Torquato, C. E. Zachary, and F. H. Stillinger, Soft Matter **7**, 3780 (2011).
- <sup>32</sup> F. H. Stillinger and T. A. Weber, Phys. Rev. A **25**, 978 (1982).
- <sup>33</sup> P. Shah and C. Chakravarty, Phys. Rev. Lett. **88**, 255501 (2002).
- <sup>34</sup> W. K. Qi, Z. Wang, Y. Han, and Y. Chen, J. Chem. Phys. **133**, 234508 (2010).
- <sup>35</sup> M. Mattarelli, G. Gasperi, M. Montagna, and P. Verrocchio, Phys. Rev. B **82**, 094204 (2010).
- <sup>36</sup> M. Mattarelli, M. Montagna, and P. Verrocchio, Appl. Phys. Lett. **91**, 061911 (2007).
- <sup>37</sup> S. Torquato, O. U. Uche, and F. H. Stillinger, Phys. Rev. E **74**, 61308 (2006).
- <sup>38</sup> A. Sütő, Phys. Rev. Lett. **95**, 265501 (2005).
- <sup>39</sup> L. Verlet, Phys. Rev. **159**, 98 (1967).
- <sup>40</sup> J. E. Dennis and H. H. W. Mei, J. Optim. Theory Appl. **28**, 453 (1979).
- <sup>41</sup> L. Kaufman, SIAM J. Optim. **10**, 56 (1999).
- <sup>42</sup> G. Henkelman and H. Jónsson, J. Chem. Phys. **113**, 9978 (2000).
- <sup>43</sup> G. Henkelman, G. Jóhannesson, and H. Jónsson, Theoret. Methods Condensed Phase Chem. pp. 269–302 (2002).
- <sup>44</sup> F. H. Stillinger, Phys. Rev. E **59**, 48 (1999).